

# ULRR

## Rayleigh-Bénard convection at high Rayleigh number and infinite Prandtl number: asymptotics and numerics

Item Type	Article
Authors	Vynnycky, Michael;Masuda, Y
Citation	Physics of Fluids;25, 113602
Publisher	American Institute of Physics
Download date	2026-06-09 20:39:20
Item License	<a href="https://creativecommons.org/licenses/by-nc-sa/1.0/">https://creativecommons.org/licenses/by-nc-sa/1.0/</a>
Link to Item	<a href="https://hdl.handle.net/10344/4557">https://hdl.handle.net/10344/4557</a>

## Rayleigh-Bénard convection at high Rayleigh number and infinite Prandtl number: Asymptotics and numerics

M. Vynnycky<sup>1,a)</sup> and Y. Masuda<sup>2</sup>

<sup>1</sup>*Mathematics Applications Consortium for Science and Industry (MACSI),  
Department of Mathematics and Statistics, University of Limerick, Limerick, Ireland*

<sup>2</sup>*Research Center for Compact Chemical Processes, National Institute of Advanced  
Industrial Science and Technology, 4-2-1 Nigatake, Miyagino-ku, Sendai 983-8551, Japan*

(Received 27 February 2013; accepted 23 October 2013;  
published online 12 November 2013)

The problem of fast viscous steady Rayleigh-Bénard convection in a rectangular enclosure is revisited using asymptotic and numerical methods. There are two generic cases: in the first, there is zero shear stress at all boundaries; in the second, there is zero shear stress at the vertical boundaries, but no slip at the horizontal ones. For the first case, we reconcile our new numerical solutions to the full equations with earlier asymptotic results for large Rayleigh number and effectively infinite Prandtl number. For the second case, we first derive the corresponding asymptotic theory and then reconcile it also with the relevant full numerical solutions. However, the latter also indicate behavior which the asymptotic theory does not predict, for Rayleigh numbers in excess of just over  $10^6$  and aspect ratios in excess of around 1.1. © 2013 AIP Publishing LLC. [<http://dx.doi.org/10.1063/1.4829450>]

### I. INTRODUCTION

The steady flow of an infinite Prandtl number Boussinesq fluid confined between a rectangular enclosure with stress-free boundaries and heated from below has come to serve as a paradigm for the natural convection in the earth's mantle that is the driving mechanism for plate tectonics. Although the relation to mantle convection has long been known to be doubtful, especially when the fluid is assumed to be isoviscous and the boundaries are stress-free, this case constitutes nevertheless the starting point for the more realistic case when the viscosity is temperature-dependent.<sup>1</sup> This is particularly the case whenever numerical computation is involved, as this example serves as a convenient benchmark.<sup>2-9</sup> A related problem which has often been discussed in tandem concerns the case when the horizontal boundaries are made no-slip instead.<sup>10-12</sup>

Whilst Roberts,<sup>10</sup> Jimenez and Zufria,<sup>11</sup> and Fowler<sup>12</sup> have tackled many analytical aspects of the problem, a number of unresolved issues remain. Jimenez and Zufria<sup>11</sup> claim that there is an error in Roberts' earlier analysis for the no-stress case, whereas Fowler<sup>12</sup> claims that there is an error in Roberts' analysis for the no-slip case. Furthermore, Jimenez and Zufria<sup>11</sup> claim that the problem for the case with no-slip horizontal walls has no solution, but do not provide details. Their inference is that the boundary-layer approximation fails, which Fowler<sup>12</sup> deems a hazardous conclusion, whilst giving suggestions as to how the boundary-layer and plume structure should look like. Also of relevance to the no-slip case are the papers of Grossmann and Lohse;<sup>19,20</sup> we return to these in more detail later. Other recent related work is due to Chini and Cox,<sup>13</sup> although they consider the problem for finite values of the Prandtl number. Jimenez and Zufria<sup>11</sup> also compared their boundary-layer solution with earlier numerical results,<sup>14-18</sup> although the latter were not computed at high enough Rayleigh number in order to enable a meaningful comparison to be made. In summary, there is no clear agreement as to what the solutions to the two problems actually are.

<sup>a)</sup> Author to whom correspondence should be addressed. Electronic mail: [michael.vynnycky@ul.ie](mailto:michael.vynnycky@ul.ie). Tel.: +353 61 233735.

Our purpose here is twofold: to provide the supplementary numerical results that finally complete the solution to the problem with stress-free horizontal boundaries; then, to unify the asymptotics and numerics for the modified problem with no-slip horizontal boundaries. The layout of the paper is as follows. In Sec. II, we formulate the problem and nondimensionalize the governing equations. In Sec. III, we consider the asymptotic solution for the no-slip case; this yields a coupled problem, that links the core flow to that in the thermal boundary layers and the plumes, which must be solved numerically. The details of the two sets of numerical work in this paper — the solution of the full equations for both cases and those of the asymptotic model for the no-slip case — are given in Sec. IV. In Sec. V, we present the results for both the no-shear and the no-slip cases; we demonstrate excellent agreement with Jimenez and Zufiria's asymptotic solution<sup>11</sup> and our own asymptotic solution in Sec. III, respectively. However, we also observe that the full numerical solutions for the no-slip case can give enclosure aspect ratio-dependent behavior that is not predicted by the asymptotic theory. Finally, conclusions are drawn in Sec. VI.

## II. PROBLEM FORMULATION

A schematic for the problem is given in Fig. 1, which shows one of a series of periodically repeating Bénard cells of height  $H$  and width  $W$ . The horizontal boundaries at  $y = 0$  and  $H$  are at temperatures  $T_h$  and  $T_c$ , respectively, where  $T_h > T_c$ , and are subject to no slip or no tangential shear, whereas  $x = 0$  and  $W$  constitute symmetry boundaries.

In primitive variable form, the equations of thermal convection with the Boussinesq approximation and neglecting the inertia terms in the Navier-Stokes equations, which corresponds to the assumption of infinite Prandtl number, are then

$$u_x + v_y = 0, \quad (1)$$

$$0 = -p_x + \mu (u_{xx} + u_{yy}), \quad (2)$$

$$0 = -p_y + \mu (v_{xx} + v_{yy}) + \rho_0 g \alpha (T - T_0), \quad (3)$$

$$\rho_0 c_p (uT_x + vT_y) = k (T_{xx} + T_{yy}), \quad (4)$$

where  $\mu$  is the viscosity,  $\rho_0$  is a reference density,  $T_0$  is a reference temperature,  $k$  is the thermal conductivity,  $c_p$  is the specific heat capacity,  $\alpha$  is the thermal expansion coefficient, and  $g$  is the

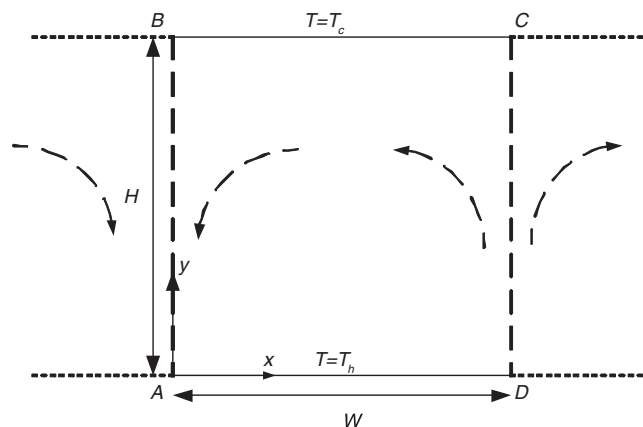


FIG. 1. Geometry of the flow.

acceleration due to gravity. The boundary conditions are

$$v = 0, \quad u_y = 0, \quad T = T_h \quad \text{at } y = 0, \quad 0 \leq x \leq W, \quad (5)$$

$$v = 0, \quad u_y = 0, \quad T = T_c \quad \text{at } y = H, \quad 0 \leq x \leq W, \quad (6)$$

$$u = 0, \quad v_x = 0, \quad T_x = 0 \quad \text{at } x = 0, \quad 0 \leq y \leq H, \quad (7)$$

$$u = 0, \quad v_x = 0, \quad T_x = 0 \quad \text{at } x = W, \quad 0 \leq y \leq H. \quad (8)$$

In tandem with the problems posed by Eqs. (1)–(4) subject to (5)–(8), we will also consider what happens when no-slip conditions are applied at  $y = 0$  and  $H$ ; in this case, boundary conditions (5) and (6) will be replaced by

$$u = 0, \quad v = 0, \quad T = T_h, \quad (9)$$

$$u = 0, \quad v = 0, \quad T = T_c, \quad (10)$$

respectively.

We nondimensionalize by writing

$$\tilde{x} = \frac{x}{H}, \quad \tilde{y} = \frac{y}{H}, \quad \tilde{u} = \frac{u}{k/H\rho_0 c_p}, \quad \tilde{v} = \frac{v}{k/H\rho_0 c_p}, \quad \tilde{p} = \frac{p}{H^2\rho_0 c_p}, \quad \theta = \frac{T - T_c}{T_h - T_c}. \quad (11)$$

Equations (1)–(4) become, on dropping the tildes,

$$u_x + v_y = 0, \quad (12)$$

$$0 = -p_x + u_{xx} + u_{yy}, \quad (13)$$

$$0 = -p_y + v_{xx} + v_{yy} + Ra\theta, \quad (14)$$

$$u\theta_x + v\theta_y = \theta_{xx} + \theta_{yy}, \quad (15)$$

where the Rayleigh number,  $Ra$ , is given by

$$Ra = \frac{\alpha g \rho_0^2 c_p (T_h - T_c) H^3}{k\mu}. \quad (16)$$

The boundary conditions are

$$v = 0, \quad u_y = 0, \quad \theta = 1 \quad \text{at } y = 0, \quad 0 \leq x \leq \lambda, \quad (17)$$

$$v = 0, \quad u_y = 0, \quad \theta = 0 \quad \text{at } y = 1, \quad 0 \leq x \leq \lambda, \quad (18)$$

$$u = 0, \quad v_x = 0, \quad \theta_x = 0 \quad \text{at } x = 0, \quad 0 \leq y \leq 1, \quad (19)$$

$$u = 0, \quad v_x = 0, \quad \theta_x = 0 \quad \text{at } x = \lambda, \quad 0 \leq y \leq 1, \quad (20)$$

where  $\lambda = W/H$ ; when no-slip conditions are applied at  $y = 0$  and  $1$ , (17) and (18) will be replaced by

$$u = 0, \quad v = 0, \quad \theta = 1, \quad (21)$$

$$u = 0, \quad v = 0, \quad \theta = 0, \quad (22)$$

respectively.

Whilst the primitive-variable formulation description given above is useful for full numerical computation, a streamfunction-vorticity formulation is more convenient for the ensuing asymptotic analysis. For this, we define a streamfunction,  $\psi$ , through

$$u = \psi_y, \quad v = -\psi_x. \quad (23)$$

The governing equations are then written as

$$\nabla^2 \psi = -\omega, \quad (24)$$

$$\nabla^2 \omega = -Ra\theta_x, \quad (25)$$

$$\psi_y \theta_x - \psi_x \theta_y = \nabla^2 \theta, \quad (26)$$

where  $\omega (= v_x - u_y)$  is the vorticity. The boundary conditions for Eqs. (24)–(26) are

$$\psi = 0, \quad \omega = 0, \quad \theta = 1 \quad \text{at } y = 0, \quad 0 \leq x \leq \lambda, \quad (27)$$

$$\psi = 0, \quad \omega = 0, \quad \theta = 0 \quad \text{at } y = 1, \quad 0 \leq x \leq \lambda, \quad (28)$$

$$\psi = 0, \quad \omega = 0, \quad \theta_x = 0 \quad \text{at } x = 0, \quad 0 \leq y \leq 1, \quad (29)$$

$$\psi = 0, \quad \omega = 0, \quad \theta_x = 0 \quad \text{at } x = \lambda, \quad 0 \leq y \leq 1; \quad (30)$$

when no-slip conditions are applied at  $y = 0$  and  $1$ , Eqs. (27) and (28) will be replaced by

$$\psi = 0, \quad \psi_y = 0, \quad \theta = 1, \quad (31)$$

$$\psi = 0, \quad \psi_y = 0, \quad \theta = 0, \quad (32)$$

respectively.

Finally, a dimensionless number of interest that characterizes the heat transfer will be the Nusselt number,  $Nu$ , given by

$$Nu = - \int_0^\lambda \left( \frac{\partial \theta}{\partial y} \right)_{y=0} dx. \quad (33)$$

### III. ANALYSIS

The asymptotic structure of the flow when boundary conditions (27) and (28) are used has been established previously,<sup>10,11</sup> but, for completeness, it is shown in Fig. 2. This consists of an isothermal core region, vertical plumes of thickness  $O(Ra^{-1/3})$  at  $x = 0, \lambda$ , horizontal boundary

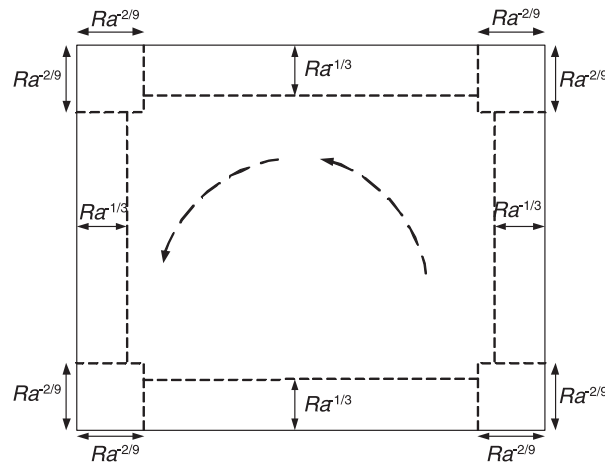


FIG. 2. Multi-region asymptotic structure of a steady Rayleigh-Bénard convection cell as  $Ra \rightarrow \infty$  when no-shear conditions are prescribed on all boundaries.

layers of thickness  $O(Ra^{-1/3})$  at  $y = 0, 1$ , and four corner layers of extent  $O(Ra^{-2/9}) \times O(Ra^{-2/9})$ . In addition,  $Nu$  is known to scale as  $Ra^{1/3}$ .<sup>10–12</sup>

For the analysis, we will focus instead on the problem when (31) and (32) are used. Before proceeding further, it is beneficial to rescale  $\psi$  and  $\omega$  through

$$\psi = \frac{\tilde{\psi}}{\epsilon^3}, \quad \omega = \frac{\tilde{\omega}}{\epsilon^3},$$

so that, although (27)–(30) remain unchanged, (24)–(26) become, on setting  $\epsilon = Ra^{-1/5}$  and once again dropping the tildes,

$$\nabla^2 \psi = -\omega, \quad (34)$$

$$\epsilon^2 \nabla^2 \omega = -\theta_x, \quad (35)$$

$$\psi_y \theta_x - \psi_x \theta_y = \epsilon^3 \nabla^2 \theta. \quad (36)$$

Roberts<sup>10</sup> and Fowler<sup>12</sup> have both given some aspects of the foregoing analysis, for example, both predict horizontal boundary layers of thickness  $Ra^{-1/5}$ , vertical plumes of thickness  $Ra^{-1/3}$  and that  $Nu \sim Ra^{1/5}$ ; we show the derivation of the latter in Appendix A. Even so, there are errors in the first work and omissions in the second, which we address here.

### A. Core

In the core, the Prandtl-Batchelor theorem and the symmetry of the flow lead to  $\theta = 1/2$ , as in the case where there is no shear at all boundaries,<sup>11</sup> whereas  $\psi$  satisfies

$$\nabla^4 \psi = 0, \quad (37)$$

and clearly the core flow cannot have  $\psi = \omega = 0$  at the boundaries for non-zero  $\psi$ . In fact,  $\psi$  jumps at the side-walls where the plume buoyancy generates a non-zero vorticity; it is therefore necessary to examine the plumes.

## B. Plumes

Near  $x = \lambda$ , for example, we rescale the variables as

$$x = \lambda - \epsilon^{3/2} X, \quad \psi = \epsilon^{3/2} \Psi, \quad \theta = \frac{1}{2} - \epsilon^{1/2} \vartheta; \quad (38)$$

the reason for choosing this scaling is given when we consider the corner regions in Sec. III D. At leading order, Eq. (34) gives

$$\Psi_{XX} \approx 0, \quad (39)$$

whence  $\Psi \sim -v_p(y) X$ , and to match to the core flow, we define  $v_p = -\psi_x|_{x=\lambda}$  as the core velocity at  $x = \lambda$ . Also, Eqs. (35) and (36) give, respectively,

$$\omega_{XX} \approx -\vartheta_X, \quad (40)$$

$$-\Psi_y \vartheta_X + \Psi_X \vartheta_y \approx \vartheta_{XX}, \quad (41)$$

the former of which integrates twice to give

$$\omega = -\int_0^X \vartheta dX, \quad \omega_p = -\int_0^\infty \vartheta dX, \quad (42)$$

where matching requires  $\omega_p$  to be the core vorticity at  $x = \lambda$ . In von Mises' coordinates  $(y, \Psi)$ , Eq. (41) becomes

$$\vartheta_\zeta = \vartheta_{\Psi\Psi}, \quad (43)$$

where  $\zeta = \int_0^y v_p(y) dy$ . Integrating once and applying the boundary conditions

$$\vartheta_\Psi = 0 \quad \text{at } \Psi = 0, \quad (44)$$

$$\vartheta \rightarrow 0 \quad \text{as } \Psi \rightarrow \infty, \quad (45)$$

gives

$$\int_0^\infty \vartheta_\zeta d\Psi = 0, \quad (46)$$

whence  $\int_0^\infty \vartheta d\Psi = \chi$ , an unknown positive constant that is to be determined; then, from the second equation in (42), it follows that the core flow must satisfy the boundary condition

$$\omega \psi_x = \chi \quad \text{on } x = \lambda. \quad (47)$$

As for  $\vartheta$ , it satisfies (43), subject to (44), (45), and

$$\vartheta = \chi \delta(\zeta), \quad (48)$$

i.e., the initial plume profile is effectively a delta function,  $\delta(\zeta)$ . The plume temperature is just the resultant similarity solution, i.e.,

$$\vartheta = \frac{\chi}{\sqrt{\pi \zeta}} \exp\left(-\frac{\Psi^2}{4\zeta}\right). \quad (49)$$

In summary, the effective boundary conditions for the core flow, and hence Eq. (37), are

$$\psi = 0 \quad \text{at } x = 0, \lambda \text{ and } y = 0, 1, \quad (50)$$

$$\psi_y = 0 \quad \text{at } y = 0, 1, \quad (51)$$

$$\psi_x \psi_{xx} = -\chi \quad \text{at } x = 0, \quad (52)$$

$$\psi_x \psi_{xx} = \chi \quad \text{at } x = \lambda, \quad (53)$$

and the solution can be found as  $\psi = \chi^{1/2} \hat{\psi}$ , where  $\hat{\psi}$  has to be computed numerically. It thus remains to determine  $\chi$ , and this requires consideration of the horizontal thermal boundary layers.

### C. Boundary layers

Consider next the layer at  $y = 0$ . Setting

$$y = \epsilon Y, \quad \psi = \epsilon^2 \Psi, \quad \omega = \omega^*, \quad (54)$$

we have

$$\omega^* = -\Psi_{YY}, \quad (55)$$

$$\omega_{YY}^* = -\theta_x, \quad (56)$$

$$\Psi_Y \theta_x - \Psi_x \theta_Y = \theta_{YY}, \quad (57)$$

subject to

$$\psi = \psi_Y = 0, \quad \theta = 1 \quad \text{at } Y = 0, \quad (58)$$

$$\omega^* \rightarrow \omega_\infty(x), \quad \theta \rightarrow \frac{1}{2} \quad \text{as } Y \rightarrow \infty, \quad (59)$$

where  $\omega_\infty(x)$  will be known, up to the constant  $\chi$ , from the core solution, i.e.,  $\omega_\infty(x) = \omega(x, 0)$ ; note that vorticity balances buoyancy in Eq. (56), an omission in Roberts' paper<sup>10</sup> which precludes the possibility of a similarity solution. Moreover, because it will be necessary to find the solution numerically, it is evident that the form of the boundary conditions for  $\psi$  and  $\omega^*$  is rather awkward: there are two conditions on  $\Psi$  at  $Y = 0$  and none as  $Y \rightarrow \infty$ , and no conditions at all on  $\omega^*$  at  $Y = 0$ . This is discussed further in Appendix B.

Although there is no similarity solution, the use of similarity-like transformations for solving these equations numerically is nonetheless essential. Setting

$$\theta = \frac{1}{2} + \frac{1}{2} \Theta(x, \eta), \quad \omega^* = \omega_\infty(x) \Omega(x, \eta), \quad \Psi = x^{1/2} \Phi(x, \eta), \quad \eta = Y/x^{1/2},$$

Eqs. (55)–(57) become

$$\omega_\infty x^{1/2} \Omega = -\Phi_{\eta\eta}, \quad (60)$$

$$2\omega_\infty \Omega_{\eta\eta} = \frac{1}{2} \eta \Theta_\eta - x \Theta_x, \quad (61)$$

$$x (\Phi_\eta \Theta_x - \Phi_x \Theta_\eta) - \frac{1}{2} \Phi \Theta_\eta = \Theta_{\eta\eta}, \quad (62)$$

subject to

$$\Phi = \Phi_\eta = 0, \quad \Theta = 1 \quad \text{at } \eta = 0, \quad (63)$$

$$\Omega \rightarrow 1, \quad \Theta \rightarrow 0 \quad \text{as } \eta \rightarrow \infty. \quad (64)$$

Consider first the behavior of these equations as  $x \rightarrow 0$ .  $\omega_\infty(x)$  will come from the solution of (37), subject to (50)–(53). Setting  $x = r \cos \theta$ ,  $y = r \sin \theta$  for a local analysis about (0,0), we find

$$\psi \sim \frac{\chi^{1/2} r^{3/2}}{2} \left( -\cos \frac{3\theta}{2} + \sin \frac{3\theta}{2} + \cos \frac{\theta}{2} - 3 \sin \frac{\theta}{2} \right), \quad (65)$$

and hence

$$\omega \sim \chi^{1/2} r^{-1/2} \left( 3 \sin \frac{\theta}{2} - \cos \frac{\theta}{2} \right), \quad (66)$$

which means that  $\omega_\infty \sim -\omega_0 x^{-1/2}$ , where  $\omega_0 = \chi^{1/2}$ . Now, in the limit as  $x \rightarrow 0$ , Eqs. (60)–(62) reduce to

$$\omega_0 = \Phi_{\eta\eta}, \quad (67)$$

$$-\frac{1}{2} \Phi \Theta_\eta = \Theta_{\eta\eta}, \quad (68)$$

$$\Omega_{\eta\eta} = 0, \quad (69)$$

giving

$$\Phi = \frac{1}{2} \omega_0 \eta^2, \quad \Omega = 1, \quad \Theta = \frac{\int_0^\infty \exp(-\frac{1}{12} \omega_0 \eta^3) d\eta}{\int_0^\infty \exp(-\frac{1}{12} \omega_0 \eta^3) d\eta}, \quad (70)$$

where

$$\int_0^\infty \exp\left(-\frac{1}{12} \omega_0 \eta^3\right) d\eta = \left(\frac{4}{9\omega_0}\right)^{1/3} \Gamma\left(\frac{1}{3}\right),$$

with  $\Gamma$  as the gamma function, given by

$$\Gamma(x) = \int_0^\infty t^{x-1} e^{-t} dt.$$

We return to the significance of the expressions in Eq. (70) after we have considered the corners.

#### D. Corners

For flow with no-shear boundary conditions, the size of all four corner regions was determined by the location at which the core solution broke down; this always happened further from the corner, i.e., sooner, than the boundary-layer solution. For no-slip boundary conditions, however, the situation is slightly different. First of all, Eq. (35) indicates that the core solution should break down when  $\epsilon^2 \omega / r_{\lambda,0}^2 \sim 1 / r_{\lambda,0}$ , where  $r_{\lambda,0}$  denotes the radial coordinate with origin at  $(\lambda, 0)$ ; on using (66), we obtain  $r_{\lambda,0} \sim Ra^{-4/15}$ . However, the boundary-layer assumption would have already broken down much sooner at  $r_{\lambda,0} \sim Ra^{-1/5}$ ; this is similarly the case at  $(0, 1)$ . On the other hand, near  $(0, 0)$  and  $(\lambda, 1)$ , the incoming plumes break down when  $r_{\lambda,1} \sim Ra^{-3/10}$ , somewhat closer to the corner than where the core solution breaks down. We consider the two types of corner in turn.

Consider first the corner at  $(\lambda, 0)$ . On using (54) and  $x = \lambda - \epsilon X$ , Eqs. (34)–(36) become

$$\Psi_{XX} + \Psi_{YY} = -\omega, \quad (71)$$

$$\epsilon (\omega_{XX} + \omega_{YY}) = \theta_X, \quad (72)$$

$$\Psi_Y \theta_X - \Psi_X \theta_Y = -\epsilon (\theta_{XX} + \theta_{YY}). \quad (73)$$

Equation (73) indicates that  $\theta = \theta(\Psi)$ , meaning that  $\int \theta d\Psi$  will be conserved, and this explains why the scaling in Eq. (38) was used. Since  $\int (\theta - 1/2) d\Psi \sim \epsilon^2$  for the boundary layer, then if we set  $[x_p]$ ,  $[\theta_p]$ , and  $[\psi_p]$  as the  $x$ -,  $\theta$ -, and  $\psi$ -scales, respectively, for the plume, then we need  $[\theta_p][\psi_p] \sim \epsilon^2$ , as well as

$$\epsilon^2 \sim [\theta_p][x_p], \quad [\psi_p][x_p] \sim \epsilon^3,$$

from Eqs. (35) and (36), respectively; this gives  $[x_p] \sim \epsilon^{3/2}$ ,  $[\theta_p] \sim \epsilon^{1/2}$ , and  $[\psi_p] \sim \epsilon^{3/2}$ , as required. Moreover, because  $\theta$  and  $\omega$  cannot satisfy the boundary conditions at  $x = \lambda$  itself, further sub-layers will be necessary to account for this; we omit the details here, as such regions are asymptotically small and do not contribute, at leading order, to the Nusselt number.

Next, consider now the corner at (0,0). Here, we set

$$x = \epsilon^{4/3} X, \quad y = \epsilon^{4/3} Y, \quad \omega = \epsilon^{-2/3} \Omega, \quad \psi = \epsilon^2 \Psi,$$

with Eqs. (34)–(36) becoming

$$\Psi_{XX} + \Psi_{YY} = -\Omega, \quad (74)$$

$$\Omega_{XX} + \Omega_{YY} = -\theta_X, \quad (75)$$

$$\Psi_Y \theta_X - \Psi_X \theta_Y = \epsilon (\theta_{XX} + \theta_{YY}), \quad (76)$$

which also indicates that  $\theta = \theta(\Psi)$ ; once again, sub-layers lying beneath the corner layer would be required to take account of the fact that  $\theta$ , as given by Eq. (76), does not satisfy the boundary conditions at  $Y = 0$ .

Finally, although the analysis for both types of corner resulted in  $\theta = \theta(\Psi)$  and a need for sub-layers, the significance for the boundary-layer and plume equations that hold on either side of the corners is different. The corner regions near (0,0) and  $(\lambda, 1)$  are much smaller in lateral extent than the boundary layers that exit them; consequently, these boundary layers can be thought of as self-starting, with the expressions in Eq. (70) constituting initial conditions. On the other hand, the corner regions near  $(\lambda, 0)$  and  $(0, 1)$  are greater in lateral extent than that of the plumes that exit them; thus, the vertical plumes see the effect of the horizontal boundary layers through the constant of proportionality,  $\chi$ , that enters at Eq. (48). Note also how the situation differs to that for the problem with horizontal no-shear boundaries: there, the vertical plumes are as thick as the horizontal boundary layers, resulting in a periodic boundary-layer equation for  $\theta$  around the whole cell;<sup>11</sup> for horizontal no-slip boundaries, the crux of the problem is the solution of the boundary-layer equations at either  $y = 0$  or  $1$ , which we turn to shortly. Thus, both problems display the periodicity that one would expect as the edge of the cell is traversed, albeit in different ways; for the problem with horizontal no-slip boundaries, it is by virtue of the fact that the boundary-layer equations are self-starting at (0,0) and  $(\lambda, 1)$ .

Analogous to Fig. 2, the overall asymptotic structure of the flow for the no-slip case is as depicted in Fig. 3.

#### IV. NUMERICAL IMPLEMENTATION

There remain three numerical tasks:

- the solution of the full equations (12)–(15), subject to (17)–(20);
- the solution of the full equations (12)–(15), subject to (19)–(22);
- the solution of the asymptotic problem derived in Sec. III.

We describe these in turn.

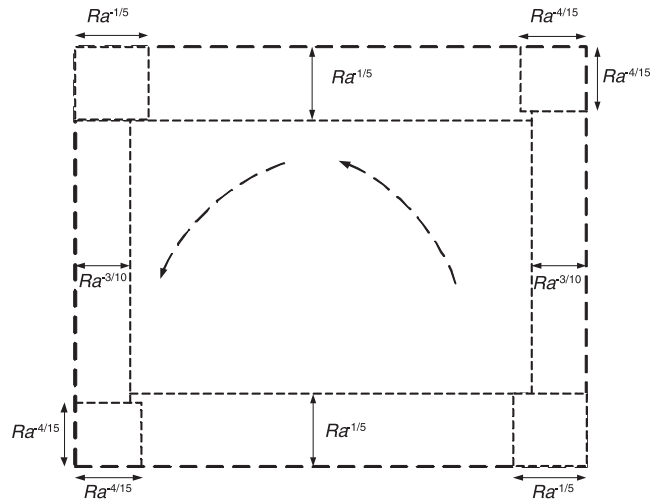


FIG. 3. Multi-region asymptotic structure of a steady Rayleigh-Bénard convection cell as  $Ra \rightarrow \infty$  when no-slip conditions are prescribed on the horizontal boundaries (and no-shear conditions on the vertical boundaries).

### A. Full equations

For these, we used the finite element-based software, Comsol Multiphysics. Lagrangian Q2-Q1 quadrilateral elements for Eqs. (24) and (25) and second-order quadrilateral elements for Eq. (26) were used on mapped non-uniform meshes having 10 000 ( $100 \times 100$ ) elements, corresponding to around 130 000 degrees of freedom. The computational mesh that was used was decided upon after a grid independence study, although, in the interest of brevity, the results of this are not presented here; the fact that we obtain good agreement with the asymptotic results means that we can be sure that we have computed accurately enough. At first sight, the principal numerical issues that must be addressed are to ensure that the boundary layers and the plumes are adequately resolved for values of  $Ra$  that are large enough for the comparison with asymptotic theory to be meaningful; the target chosen was  $Ra = 10^9$ . Over the two problems, the thinnest spatial structures are of extent  $Ra^{-1/3}$ , giving a dimensionless width of  $10^{-3}$ ; thus, the meshes that were used were refined in such a way as to ensure that five elements were located within this distance of the boundaries. The same mesh was used for both problems and for all values of  $Ra$  and  $\lambda$ , so as to enable a converged solution obtained for one value of  $Ra$  to be used as an initial guess for a new value.

As for the range in  $\lambda$  that was used, we settled for  $0.2 \leq \lambda \leq 2$ , in line with Ref. 11. An important point which enables us to find solutions for a much greater number of aspect ratios than, say, Ref. 13, is that we rescaled Eqs. (12)–(15) via  $x = \lambda \bar{x}$  to obtain

$$u_{\bar{x}} + \lambda v_y = 0, \quad (77)$$

$$0 = -\lambda p_{\bar{x}} + u_{\bar{x}\bar{x}} + \lambda^2 u_{yy}, \quad (78)$$

$$0 = -\lambda^2 p_y + v_{\bar{x}\bar{x}} + \lambda^2 v_{yy} + \lambda^2 Ra \theta, \quad (79)$$

$$\lambda u \theta_{\bar{x}} + \lambda^2 v \theta_y = \theta_{\bar{x}\bar{x}} + \lambda^2 \theta_{yy}. \quad (80)$$

This avoids the need to make a new geometry for each value of  $\lambda$  and, more importantly, allows us to use a converged solution for one value of  $\lambda$  as an initial guess for a computation for a new value; thus, in tandem with the software's multidimensional Newton solver,  $\lambda$  and  $Ra$  can both be used as

stepping parameters. For all cases, the same convergence criterion, namely,

$$\left( \frac{1}{N_{dof}} \sum_{i=1}^{N_{dof}} |E_i|^2 \right)^{1/2} < \varepsilon, \quad (81)$$

was applied; here, where  $N_{dof}$  is the number of degrees of freedom,  $E_i$  is the estimated error in the latest approximation to the  $i$ th component of the true solution vector and  $\varepsilon = 10^{-6}$ ; lower values of  $\varepsilon$  were also tried, but the results were practically indistinguishable.

Whilst the above describes the solution to the steady equations, it also proved necessary to consider the associated transient problem as a route to obtaining the solution to the steady problem. To do this, we insert the time-derivatives  $u_t$ ,  $v_t$ , and  $\theta_t$  into the left-hand sides of Eqs. (78)–(80), respectively, with  $t$  denoting time, and employ Comsol Multiphysics' transient solver. The same types of elements were employed as for the steady solver, and the convergence criterion at each time-like step was taken as

$$\left( \frac{1}{N_{dof}} \sum_{i=1}^{N_{dof}} \left( \frac{|E_i|}{A_i + R|U_i|} \right)^2 \right)^{1/2} < 1, \quad (82)$$

where ( $U_i$ ) is the solution vector corresponding to the solution at each time step,  $A_i$  is the absolute tolerance for the  $i$ th degree of freedom, and  $R$  is the relative tolerance; for the computations,  $R = 10^{-2}$ ,  $A_i = 10^{-3}$  for  $i = 1, \dots, N_{dof}$  were used.

Finally, we point out that although Comsol Multiphysics does contain a variety of numerical stabilization techniques for coupled heat and momentum transfer equations that could be of use for high values of the Rayleigh number — namely streamline, crosswind, and isotropic diffusion — we have eschewed the use of these for two reasons: to illustrate the comparative difficulty of solving the two problems; because we ultimately found that our numerical solution was able to capture the correct asymptotic behavior without us having to resort to stabilization.

## B. Asymptotic problem

The logical sequence for solving this is:

1. solve for  $\hat{\psi}$ , which satisfies

$$\nabla^4 \hat{\psi} = 0, \quad (83)$$

subject to

$$\hat{\psi} = 0 \quad \text{at } x = 0, \lambda \text{ and } y = 0, 1, \quad (84)$$

$$\hat{\psi}_y = 0 \quad \text{at } y = 0, 1, \quad (85)$$

$$\hat{\psi}_x \hat{\psi}_{xx} = -1 \quad \text{at } x = 0, \quad (86)$$

$$\hat{\psi}_x \hat{\psi}_{xx} = 1 \quad \text{at } x = \lambda; \quad (87)$$

2. make an initial guess for  $\chi$  (call it  $\chi^{(0)}$ );
3. solve Eqs. (60)–(64) for the thermal boundary layer;
4. calculate  $\int_0^\infty (\theta_{x=\lambda} - 1/2) d\Psi$  to check whether it equals  $\chi^{(0)}$ ;
5. if it does not, return to step 2, setting the new guess for  $\chi$  as  $\chi^{(1)} = \int_0^\infty (\theta_{x=\lambda} - 1/2) d\Psi$ ;
6. continue with steps 2-5 until, after some number of iterations  $n$ ,  $|\chi^{(n)} - \chi^{(n-1)}| < \varepsilon_\chi$ , where  $\varepsilon_\chi$  is a prescribed tolerance, e.g.,  $10^{-6}$ .

The numerical solution of (83) subject to (84)–(87) is discussed in Appendix C. Turning instead to the solution of Eqs. (60)–(64), we note first that there will be difficulties as we approach  $x = \lambda$ , because  $\omega_\infty \sim (\lambda - x)^{-1/2}$ , meaning that the left-hand side in Eq. (60) becomes unbounded. It is therefore advisable to preempt the problem by defining the variable

$$\bar{\eta} = \eta / (\lambda - x)^{1/4}, \quad (88)$$

so that Eqs. (60)–(64) become

$$\omega_\infty (\lambda - x)^{1/2} x^{1/2} \Omega = -\Phi_{\bar{\eta}\bar{\eta}}, \quad (89)$$

$$\Omega_{\bar{\eta}\bar{\eta}} = \frac{(\lambda - x)^{1/2}}{2\omega_\infty} \left( \frac{1}{2} \bar{\eta} \Theta_{\bar{\eta}} - x \left( \Theta_x + \frac{\bar{\eta} \Theta_{\bar{\eta}}}{4(\lambda - x)} \right) \right), \quad (90)$$

$$x (\Phi_{\bar{\eta}} \Theta_x - \Theta_{\bar{\eta}} \Phi_x) - \frac{1}{2} \Phi \Theta_{\bar{\eta}} = \frac{\Theta_{\bar{\eta}\bar{\eta}}}{(\lambda - x)^{1/4}}, \quad (91)$$

subject to

$$\Phi = \Phi_{\bar{\eta}} = 0, \quad \Theta = 1 \quad \text{at } \bar{\eta} = 0, \quad (92)$$

$$\Omega \rightarrow 1, \quad \Theta \rightarrow 0 \quad \text{as } \bar{\eta} \rightarrow \infty. \quad (93)$$

However, this still does not appear to be adequate since, if all the terms are now finite, then Eq. (91) will tend to

$$\Theta_{\bar{\eta}\bar{\eta}} = 0$$

as  $x \rightarrow \lambda$ , which would be incompatible with the boundary conditions for  $\Theta$  in Eqs. (92) and (93). This suggests that  $(\lambda - x)^{1/4} \Theta_x$  and  $(\lambda - x)^{1/4} \Phi_x$  are both finite and non-zero; hence, it is appropriate to introduce the transformation

$$\varphi = \lambda^{1/4} (\lambda^{3/4} - (\lambda - x)^{3/4}), \quad (94)$$

so that (89)–(91) become

$$\frac{\omega_\infty (\lambda - \varphi)^{2/3}}{\lambda^{1/3}} (\lambda^{4/3} - (\lambda - \varphi)^{4/3})^{1/2} \Omega = -\Phi_{\bar{\eta}\bar{\eta}}, \quad (95)$$

$$\frac{(\lambda - \varphi)^{2/3}}{4\lambda^{1/6}\omega_\infty} \left( \bar{\eta} \Theta_{\bar{\eta}} - \frac{1}{2} \left( \frac{\lambda^{4/3}}{(\lambda - \varphi)^{4/3}} - 1 \right) (3(\lambda - \varphi) \Theta_\varphi + \bar{\eta} \Theta_{\bar{\eta}}) \right) = \Omega_{\bar{\eta}\bar{\eta}}, \quad (96)$$

$$\frac{3}{4} (\lambda^{4/3} - (\lambda - \varphi)^{4/3}) (\Phi_{\bar{\eta}} \Theta_\varphi - \Theta_{\bar{\eta}} \Phi_\varphi) - \frac{1}{2} (\lambda - \varphi)^{1/3} \Phi \Theta_{\bar{\eta}} = \lambda^{1/12} \Theta_{\bar{\eta}\bar{\eta}}, \quad (97)$$

with (92) and (93) remaining unchanged. This time, all terms in the governing equations, (95)–(97), are finite as the end of the thermal boundary layer is approached, i.e., as  $\varphi \rightarrow \lambda$ ; in this limit, we have

$$\lambda^{1/2} \omega_0 \Omega = \Phi_{\bar{\eta}\bar{\eta}}, \quad (98)$$

$$\frac{\lambda}{8\omega_0} \bar{\eta} \Theta_{\bar{\eta}} = \Omega_{\bar{\eta}\bar{\eta}}, \quad (99)$$

$$\frac{3}{4} \lambda^{5/4} (\Phi_{\bar{\eta}} \Theta_\varphi - \Theta_{\bar{\eta}} \Phi_\varphi) = \Theta_{\bar{\eta}\bar{\eta}}. \quad (100)$$

At this point, we note that the Nusselt number, as defined in Eq. (33), is given in transformed variables by

$$Nu = -\frac{2Ra^{1/5}}{3\lambda^{1/6}} \int_0^\lambda \frac{(\lambda - \varphi)^{1/3} \Theta_{\bar{\eta}}(\varphi, 0) d\varphi}{(\lambda^{4/3} - (\lambda - \varphi)^{4/3})^{1/2}}, \quad (101)$$

which has an integrable singularity at  $\varphi = 0$ , since the integrand in (101) behaves as  $\varphi^{-1/2}$  as  $\varphi \rightarrow 0$ . This is remedied by using  $\xi := \varphi^{1/2}$  instead, which gives

$$Nu = -\frac{4Ra^{1/5}}{3\lambda^{1/6}} \int_0^{\lambda^{1/2}} \frac{(\lambda - \xi^2)^{1/3} \xi \Theta_{\bar{\eta}}(\xi, 0) d\xi}{(\lambda^{4/3} - (\lambda - \xi^2)^{4/3})^{1/2}}, \quad (102)$$

whereas Eqs. (89)–(93) become

$$\frac{\omega_\infty (\lambda - \xi^2)^{2/3}}{\lambda^{1/3}} (\lambda^{4/3} - (\lambda - \xi^2)^{4/3})^{1/2} \Omega = -\Phi_{\bar{\eta}\bar{\eta}}, \quad (103)$$

$$\frac{(\lambda - \xi^2)^{2/3}}{4\lambda^{1/6}\omega_\infty} \left( \bar{\eta}\Theta_{\bar{\eta}} - \frac{1}{2} \left( \frac{\lambda^{4/3}}{(\lambda - \xi^2)^{4/3}} - 1 \right) \left( \frac{3}{2\xi} (\lambda - \xi^2) \Theta_\xi + \bar{\eta}\Theta_{\bar{\eta}} \right) \right) = \Omega_{\bar{\eta}\bar{\eta}}, \quad (104)$$

$$\frac{3}{8\xi} (\lambda^{4/3} - (\lambda - \xi^2)^{4/3}) (\Phi_{\bar{\eta}}\Theta_\xi - \Theta_{\bar{\eta}}\Phi_\xi) - \frac{1}{2} (\lambda - \xi^2)^{1/3} \Phi\Theta_{\bar{\eta}} = \lambda^{1/12}\Theta_{\bar{\eta}\bar{\eta}}, \quad (105)$$

subject to

$$\Phi = \Phi_{\bar{\eta}} = 0, \quad \Theta = 1 \quad \text{at } \bar{\eta} = 0, \quad (106)$$

$$\Omega \rightarrow 1, \quad \Theta \rightarrow 0 \quad \text{as } \bar{\eta} \rightarrow \infty, \quad (107)$$

with  $\chi$  being given by

$$\chi = \frac{1}{2} \int_0^\infty (\Theta\Phi_{\bar{\eta}})_{\xi=\lambda^{1/2}} d\bar{\eta}. \quad (108)$$

thus, of the five forms of the boundary-layer equations that have been given, i.e., (55)–(59), (60)–(64), (89)–(93), (95)–(97), and (103)–(105), the last of these is best-suited for delivering the numerical value of  $Nu$ . Finally, in line with the discussion in Appendix B, we remark that we implement boundary conditions (106) and (107) in the form: at  $\bar{\eta} = 0$ ,

$$\Phi = 0, \quad \Theta = 1, \quad (109)$$

$$\Omega_{\bar{\eta}} = -\frac{(\lambda - \xi^2)^{2/3}}{2\lambda^{1/6}\omega_\infty} \left( \frac{1}{4} \left( \frac{\lambda^{4/3}}{(\lambda - \xi^2)^{4/3}} - 1 \right) \left( \frac{3}{2\xi} (\lambda - \xi^2) I_1(\xi) + I_2(\xi) \right) - \frac{1}{2} I_2(\xi) \right), \quad (110)$$

where

$$I_1(\xi) = \int_0^\infty \Theta_\xi d\bar{\eta}, \quad I_2(\xi) = \int_0^\infty \bar{\eta}\Theta_{\bar{\eta}} d\bar{\eta};$$

as  $\bar{\eta} \rightarrow \infty$ ,

$$\Phi_{\bar{\eta}} \sim -\frac{\omega_\infty (\lambda - \xi^2)^{2/3}}{\lambda^{1/3}} (\lambda^{4/3} - (\lambda - \xi^2)^{4/3})^{1/2} \bar{\eta} + A(\xi), \quad (111)$$

$$\Omega \rightarrow 1, \quad \Theta \rightarrow 0, \quad (112)$$

where  $A(\xi)$  in Eq. (111) is iterated on until

$$\Phi_{\bar{\eta}} = 0 \quad \text{at } \bar{\eta} = 0. \quad (113)$$

For the numerical solution of equations (103)–(105) subject to (70) and (109)–(113), the 1D transient mode of Comsol Multiphysics was used, with  $\xi$  as the time-like variable. Once again, second-order elements were employed, with the outer edge of the computational domain taken at  $\bar{\eta} = 20$ , which was found to be more than sufficient; grid independence was obtained by using 960 elements in  $\bar{\eta}$ , corresponding to around 5800 degrees of freedom. The convergence criterion at each time-like step was of the same form as in (82).

## V. RESULTS

### A. No-shear boundary conditions at $y = 0, 1$

Fig. 4 shows  $Nu/\lambda Ra^{1/3}$  vs.  $\lambda$  for three values of  $Ra$  and compares our computations with the asymptotic result of Jimenez and Zufiria.<sup>11</sup> We see that there is considerably better agreement between asymptotic and numerical results than was previously the case,<sup>11,14–18</sup> even so far as capturing the maximum in  $Nu/\lambda Ra^{1/3}$  near  $\lambda = 1$ ; the results strengthen the claim made in Ref. 11 that Roberts' result<sup>10</sup> was incorrect.

Fig. 5 shows  $Nu/\lambda Ra^{1/3}$  vs.  $Ra$  for  $\lambda = 0.2, 1$  and  $2$ ; the purpose of this is to see whether  $Nu/\lambda Ra^{1/3}$  is actually approaching the limiting value as  $Ra \rightarrow \infty$ , and indeed this does appear to be the case.

Furthermore, in order to help explain the anomalies that arise in the later results for the no-slip case, we present also the profiles for  $(-\theta_y)_{y=0}/Ra^{1/3}$  for  $Ra = 10^7, 10^8, 10^9$  when  $\lambda = 3/2$ ; this is given in Fig. 6. There is no untoward behavior, with the mesh used clearly being able to resolve the heat flux without any difficulty.

### B. No-slip boundary conditions at $y = 0, 1$

Fig. 7 shows results obtained for  $Ra = 10^6, 5 \times 10^6$ , and  $10^7$  using the steady solver. Whilst the curve for  $Ra = 10^6$  is continuous, the curves for  $Ra = 5 \times 10^6$  and  $10^7$  each have two branches. For all three values of  $Ra$ , a converged solution was first obtained for  $\lambda = 0.2$  at a low value of  $Ra$ , for which the problem is fairly linear; the value of  $Ra$  was then increased to the desired value, from which we stepped up in values of  $\lambda$  up to  $\lambda = 2$ . For  $Ra = 10^6$ , it was possible to step all the way to

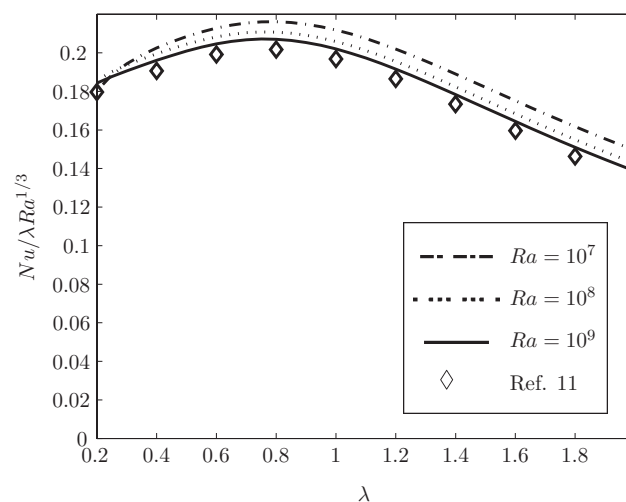


FIG. 4.  $Nu/\lambda Ra^{1/3}$  vs.  $\lambda$  for  $Ra = 10^7, 10^8, 10^9$  and comparison with Ref. 11.

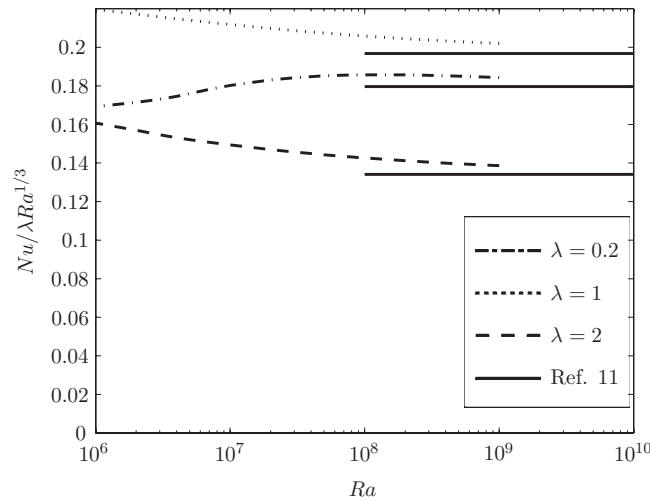


FIG. 5.  $Nu/\lambda Ra^{1/3}$  vs.  $Ra$  for  $\lambda = 0.2, 1,$  and  $2$ .

$\lambda = 2$ , but for the higher values of  $Ra$ , there appeared to be a critical value of  $\lambda$ , above which it was not possible to step. However, there is clearly more than one route to attempting to obtain converged solutions for, say,  $\lambda = 2$  and  $Ra = 10^7$ : instead of the one already mentioned, one could simply start at  $\lambda = 2$  for a low value of  $Ra$ , and then progressively increase it up to  $Ra = 10^7$ . Subsequently, one could then decrease  $\lambda$ , and hope to reproduce the same  $Nu/\lambda Ra^{1/5}$  or  $Nu/\lambda Ra^{1/3}$  vs.  $\lambda$  curve as one would have obtained had one started at  $\lambda = 0.2$ . Indeed, this is what happens for the no-shear case, although not for the no-slip case for high enough values of  $Ra$ . It is this procedure that has led to the two lower branches for  $Ra = 5 \times 10^6$  and  $10^7$ .

Moreover, for these two values of  $Ra$ , it is clear that there is a range in  $\lambda$  over which there appears to be more than one steady solution. To explore this further, we carried out runs using the transient solver for  $Ra = 10^7$  and  $\lambda = 1, 1.3,$  and  $1.6$ ; we chose these values of  $\lambda$  as they lie, respectively, before, in the middle of and after the interval in which there appeared to be more than one steady solution. For all three cases, we used as initial condition the converged unique steady solution for  $Ra = 10^6$ . We found that whereas the runs for  $\lambda = 1$  and  $\lambda = 1.6$  gave the unique solution already described in Fig. 7, the run for  $\lambda = 1.3$  gave a transient solution; Fig. 8 shows  $Nu/\lambda Ra^{1/5}$  as

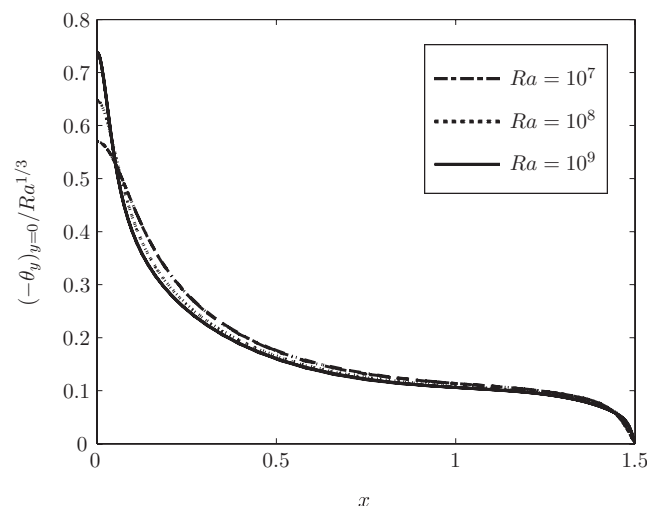


FIG. 6.  $(-\theta_y)_{y=0}/Ra^{1/3}$  vs.  $x$  for  $Ra = 10^7, 10^8, 10^9$  with  $\lambda = 3/2$  and no-shear boundary conditions at  $y = 0, 1$ .

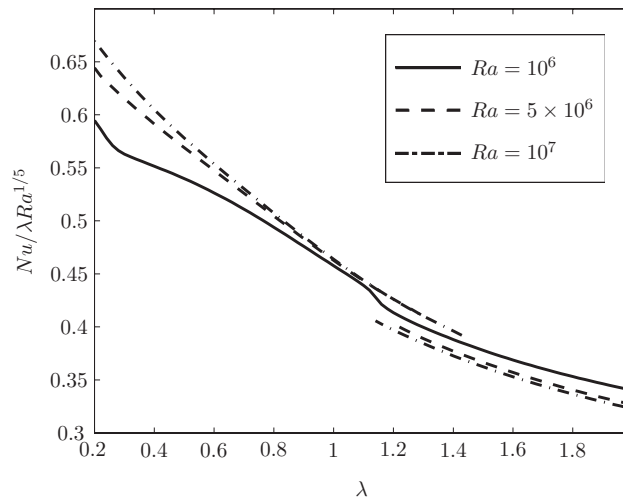


FIG. 7.  $Nu/\lambda Ra^{1/5}$  vs.  $\lambda$  for  $Ra = 10^6, 5 \times 10^6, 10^7$ .

a function of time for this case. Consequently, it is reasonable to suppose that the interval in  $\lambda$  for which the steady state solver gives non-unique solutions is where there is only a transient solution. Furthermore, the fact that this interval is shorter for  $Ra = 5 \times 10^6$  than for  $Ra = 10^7$ , as shown in Fig. 7, indicates that, as  $Ra$  increases, there is an ever-widening range of values of  $\lambda$  within which there can only be a transient solution. These results suggest a solution structure in  $(\lambda, Ra)$ -space as shown in Fig. 9: for  $Ra < Ra_c$ , where  $Ra_c$  is a critical value of  $Ra$  that, from Fig. 7, must lie between  $10^6$  and  $5 \times 10^6$ , there is a steady solution for all values of  $\lambda$ ; for  $Ra \geq Ra_c$ , there is an interval of  $\lambda$ -values starting from  $\lambda_c$ , which lies between 1.2 and 1.4, within which there are only transient solutions; outside this interval, there is unique steady solution.

As a caveat to these results, it is worth noting the combined use of steady and transient solvers, rather than one or the other, is beneficial. The steady solver is much quicker to run, but is clearly unable to interpret the meaning of apparently non-unique solutions. On the other hand, the range in  $\lambda$  values for which such solutions are obtained does serve to determine the interval in  $\lambda$  for which there is only a transient solution, which can then be verified *a posteriori* using the transient solver.

Fig. 10 shows  $Nu/\lambda Ra^{1/5}$  vs.  $\lambda$  for  $Ra = 10^7$  and  $10^8$ , and compares our computations with Eq. (102) and that of Roberts;<sup>10</sup> in addition, Fig. 11 shows  $\chi$  as a function of  $\lambda$  in our asymptotic solution. There are several features to observe here:

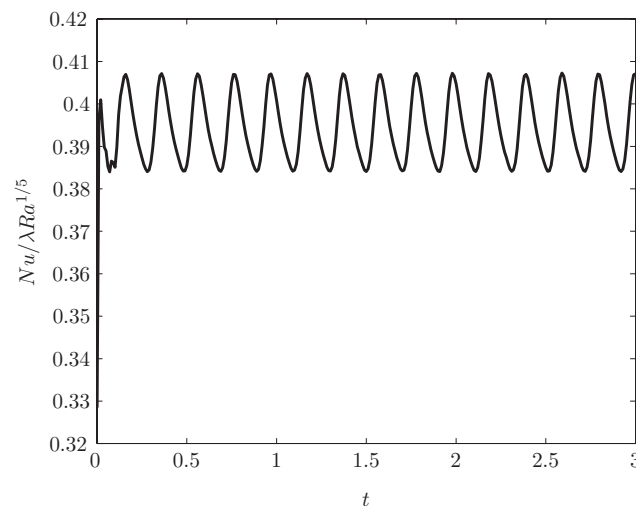


FIG. 8.  $Nu/\lambda Ra^{1/5}$  vs.  $t$  for  $Ra = 10^7, \lambda = 1.3$ .

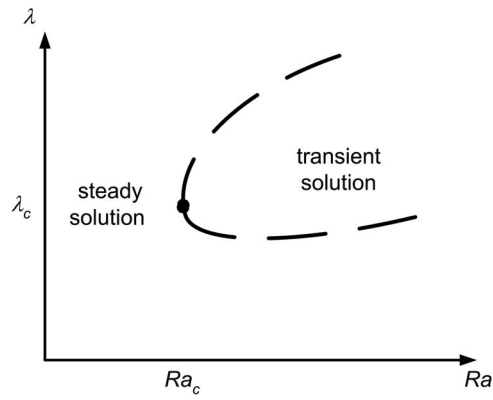


FIG. 9. Proposed solution structure in  $(\lambda, Ra)$ -space for the no-slip case.

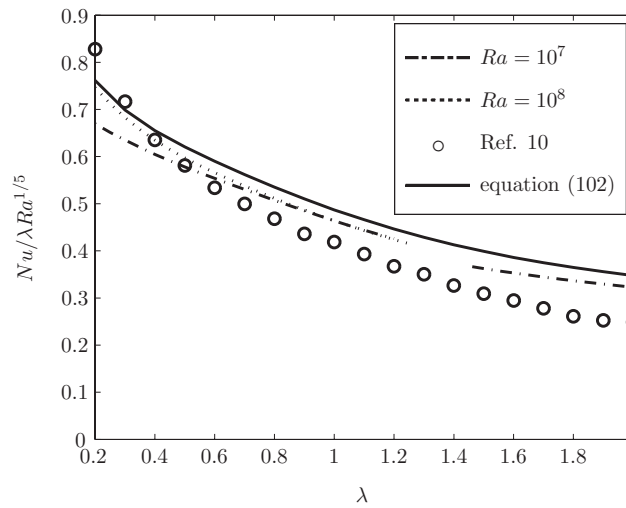


FIG. 10.  $Nu/\lambda Ra^{1/5}$  vs.  $\lambda$  for  $Ra = 10^7, 10^8$  and comparison with Ref. 10.

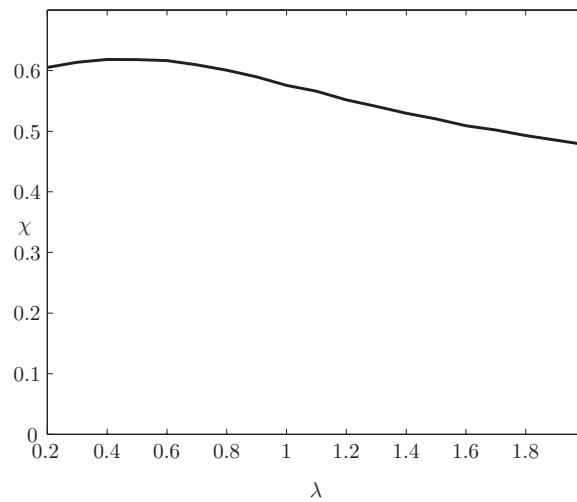


FIG. 11.  $\chi$  vs.  $\lambda$  for our asymptotic solution.

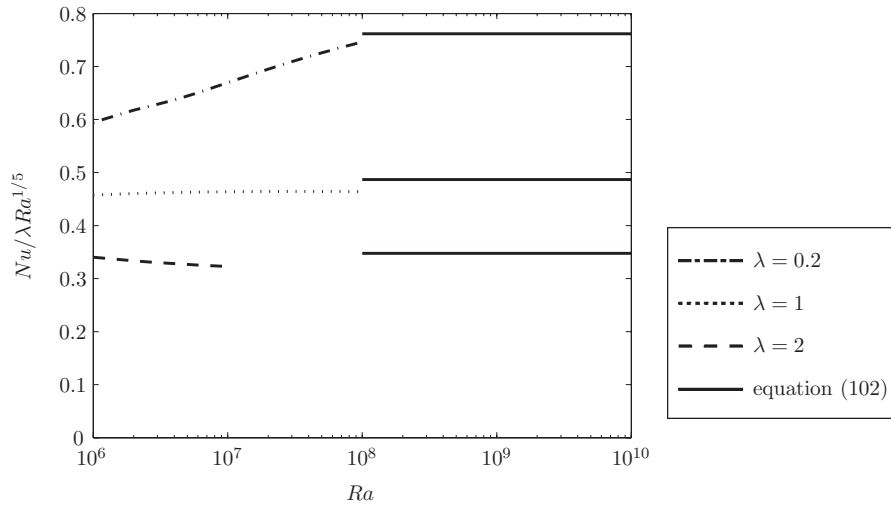


FIG. 12.  $Nu/\lambda Ra^{1/5}$  vs.  $Ra$  for  $\lambda = 0.2, 1,$  and  $2.$

- In view of the discussion concerning steady and transient solutions, we have only plotted the steady state solutions for  $Ra = 10^7$  and  $10^8$ . This accounts for the gap in the curve for  $Ra = 10^7$ .
- For  $Ra = 10^8$ , there is a transient solution for  $\lambda \gtrsim 1.24$ , which explains why there is no second branch for higher values of  $\lambda$ .
- Although Fig. 7 may suggest that the onset of the transient solution occurs for lower values of  $\lambda$  as  $Ra$  is increased, this appears not to be the case; in this figure, it occurs for a higher value for  $Ra = 10^8$  than for  $Ra = 10^7$ .
- There is excellent agreement between the results for  $Ra = 10^7$  and  $10^8$  for  $0.6 \leq \lambda \leq 1.2$ . For  $0.2 \leq \lambda \leq 1$ , there is good agreement between the results for  $Ra = 10^8$  and Eq. (102), indicating that the numerical computations are resolving the asymptotic limit rather well.
- Roberts' solution<sup>10</sup> agrees quite well with the full numerical computations for  $\lambda \lesssim 0.5$ , but thereafter considerably underestimates the value of  $Nu/\lambda Ra^{1/5}$ .

Corresponding to Fig. 5 for the no-shear case, Fig. 12 shows  $Nu/\lambda Ra^{1/5}$  vs.  $Ra$  for  $\lambda = 0.2, 1,$  and  $2.$  Although agreement between the numerical and asymptotic solutions is perhaps not as

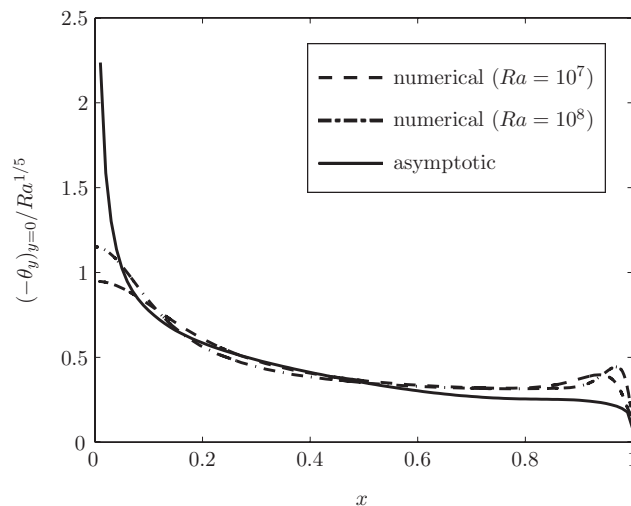


FIG. 13.  $(-\theta_y)_{y=0}/Ra^{1/5}$  vs.  $x$  for  $Ra = 10^7$  and  $10^8$  with  $\lambda = 1$  and no-slip boundary conditions at  $y = 0, 1.$

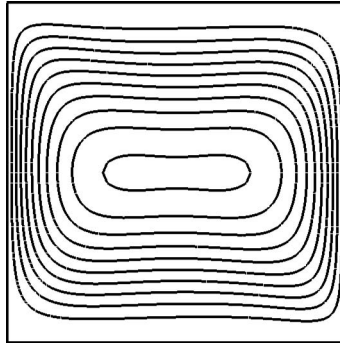


FIG. 14. Streamfunction,  $\psi$ , for the upper solution for  $Ra = 10^7$  with  $\lambda = 1$  and no-slip boundary conditions at  $y = 0, 1$  ( $-100 \leq \psi \leq 0$  with  $\Delta\psi = 10$ ). The flow is anti-clockwise.

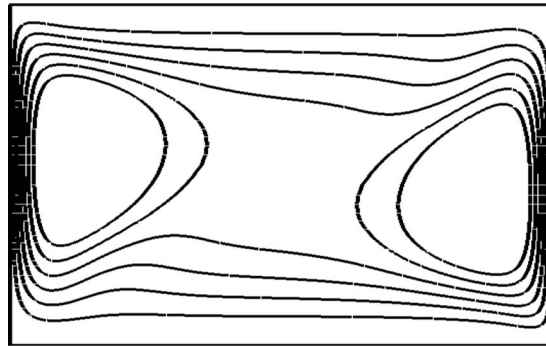


FIG. 15. Streamfunction,  $\psi$ , for the lower solution for  $Ra = 10^7$  with  $\lambda = 1.6$  and no-slip boundary conditions at  $y = 0, 1$  ( $-180 \leq \psi \leq 0$  with  $\Delta\psi = 30$ ). The flow is anti-clockwise.

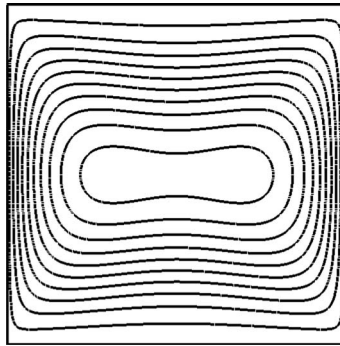


FIG. 16. Streamfunction,  $\hat{\psi}$ , for the core solution with  $\lambda = 1$ .

convincing as for the no-shear case, it is nonetheless reasonable for  $\lambda = 0.2$  and  $1$ . For  $\lambda = 2$ , it is evident from Figs. 7 and 10 that there will be an onset to a transient solution for some value of  $Ra$  between  $10^7$  and  $10^8$ ; hence, we have truncated this curve at  $Ra = 10^7$ . Fig. 13 compares the profiles of  $(-\theta_y)_{y=0}/Ra^{1/5}$  vs.  $x$  for  $Ra = 10^7, 10^8$  and  $\lambda = 1$  with the asymptotic solution for  $\lambda = 1$ . The agreement is generally good, although not so near the corners, as might be expected; nevertheless, these are asymptotically small regions, which do not impact at leading order on the Nusselt number, as already shown in Fig. 10.

Finally, it turns out to be instructive to consider the streamfunction,  $\psi$ , for a given value of  $Ra$  and two values of  $\lambda$  that are either side of the transient solution region in Fig. 10; for this purpose, we take  $Ra = 10^7$  and  $\lambda = 1, 1.6$ . Fig. 14, for  $\lambda = 1$ , shows that  $\psi$  is symmetric about the vertical centerline, whereas Fig. 15, for  $\lambda = 1.6$ , shows  $\psi$  to be skew-symmetric. By comparison, Figs. 16

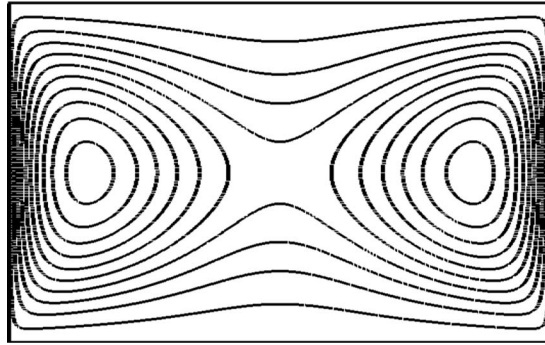


FIG. 17. Streamfunction,  $\hat{\psi}$ , for the core solution with  $\lambda = 1.6$ .

and 17 show  $\hat{\psi}$  for  $\lambda = 1$  and 1.6; in both cases,  $\hat{\psi}$  is symmetric. From this, we conclude that the asymptotic solution that we have obtained in this paper is only valid for values of  $\lambda$  that are smaller than the transient onset value.

## VI. CONCLUSIONS

This paper has revisited, both asymptotically and numerically, the problem of fast steady Rayleigh-Bénard convection at infinite Prandtl number in a rectangular enclosure of varying aspect ratio,  $\lambda$ . There are two generic cases: (i) zero shear stress at all boundaries; (ii) zero shear stress at the vertical boundaries, but no slip at the horizontal ones. Although these cases had been considered previously by others,<sup>10-12</sup> there was neither qualitative agreement on the asymptotic structure of the solution, nor quantitative agreement between asymptotic and numerical results. For (i), we have reconciled our new numerical solutions with the asymptotic results of Jimenez and Zufria,<sup>11</sup> whereas, for (ii), we have provided both asymptotic and numerical solutions that agree well with each other. Problem (ii) was found to be the more complex of the two, because of aspect ratio intervals for which there was no steady solution. Thus, whilst a steady-state numerical solver is expedient for a wide-ranging parameter study in  $\lambda$  and the Rayleigh number,  $Ra$ , a transient solver is also necessary in order to ascertain which  $(\lambda, Ra)$ -combinations give genuine steady-state solutions.

We note also how our work relates to that of Grossmann and Lohse,<sup>19,20</sup> who produced a partition of  $Ra-Pr$  parameter space, where their regime  $I_\infty^>$  corresponds to the no-slip asymptotic result derived here; moreover, it can be seen that increasing further the Rayleigh number, to above  $10^9$  or so, leads to another regime,  $III_\infty$ , that involves turbulent boundary layers and for which a different  $Nu$  scaling law holds. Furthermore, and in light of the findings in Refs. 19 and 20, it is necessary to re-assess in what sense the solutions we have found here can be considered as exhibiting *asymptotic* behaviour: although this phrase may convey the idea that the theory should apply better the higher the value of  $Ra$  becomes, in practice the limit is at around  $Ra \sim 10^9$ .

Finally, it is worth pointing out explicitly the significance of our findings regarding steady and transient solutions for the benchmarking of numerical codes in the context of mantle convection.<sup>2-9</sup> Our results indicate that, for some values of  $\lambda$  and  $Ra$ , it is possible that a steady-state code will compute a converged solution, even though there is only a transient solution for that  $(\lambda, Ra)$ -combination. Consequently, the only way to be sure is to carry out a transient computation, although, in our experience, this leads to far greater computational expense, particularly for  $(\lambda, Ra)$ -combinations that do have a genuine steady state solution.

## ACKNOWLEDGMENTS

The first author (M.V.) wishes to acknowledge the support of the Mathematics Applications Consortium for Science and Industry ([www.macsi.ul.ie](http://www.macsi.ul.ie)) funded by the Science Foundation Ireland

Mathematics Initiative, Grant No. 06/MI/005, as well as discussions with Professor A. C. Fowler and T. Khaleque. Both authors acknowledge the comments of an anonymous referee.

### APPENDIX A: DEPENDENCE OF $Nu$ ON $Ra$ FOR $Ra \gg 1$

We need to consider the behavior of Eqs. (12)–(15) near either  $y = 0$  or  $y = 1$ ; without loss of generality, we consider  $y = 0$ . These equations have to be solved in tandem with the boundary conditions in Eq. (21). When  $Ra \gg 1$ , it is evident that (14) reduces to  $\theta \approx 0$ , so that the third condition in (21) is not satisfied; hence, we require a boundary layer in  $y$ . We set

$$y = [y]Y, \quad u = [u]U, \quad v = [v]V, \quad p = [p]P,$$

where  $[y]$  is the thickness of the boundary layer, and  $[u], [v]$ , and  $[p]$  are the scales for  $u$ ,  $v$  and  $p$ , respectively, in the boundary layer; here,  $[p]$ ,  $[u]$ ,  $[v]$ , and  $[y]$  are all to be determined, and we expect  $[y] \ll 1$ . In addition,  $P, U, V, Y \sim O(1)$ , and we will also have  $x, \theta \sim O(1)$ .

Equations (12)–(15) become, respectively,

$$U_x + \left( \frac{[u]}{[v][y]} \right) V_Y = 0, \quad (\text{A1})$$

$$0 = -[p][y]^2 P_x + [u]([y]^2 U_{xx} + U_{YY}), \quad (\text{A2})$$

$$0 = -[p][y] P_Y + [v]([y]^2 V_{xx} + V_{YY}) + Ra [y]^2 \theta, \quad (\text{A3})$$

$$[u][y]^2 \left( U\theta_x + \left( \frac{[v]}{[u][y]} \right) V\theta_Y \right) = [y]^2 \theta_{xx} + \theta_{YY}. \quad (\text{A4})$$

In order to obtain self-consistent leading-order balances for all equations, we need

$$\frac{[u]}{[v][y]} \sim 1, \quad [u][y]^2 \sim 1, \quad [p][y]^2 \sim [u], \quad [p][y] \sim [v] \sim Ra [y]^2,$$

which leads to

$$[y] \sim Ra^{-1/5}, \quad [u] \sim Ra^{2/5}, \quad [v] \sim Ra^{3/5}, \quad [p] \sim Ra^{4/5};$$

so, Eqs. (A1)–(A4) become, at leading order,

$$U_x + V_Y = 0, \quad (\text{A5})$$

$$0 = -P_x + U_{YY}, \quad (\text{A6})$$

$$0 = -P_Y + V_{YY} + \theta, \quad (\text{A7})$$

$$U\theta_x + V\theta_Y = \theta_{YY}, \quad (\text{A8})$$

which is the primitive variable form of Eqs. (55)–(57).

Finally, from the definition of  $Nu$  in Eq. (33), we see that  $Nu \sim [y]^{-1}\theta_Y$ , whence  $Nu \sim Ra^{1/5}$ .

**APPENDIX B: ANALYTICAL BEHAVIOR OF THE SOLUTION TO EQS. (55) AND (56)**

To illustrate how to apply boundary conditions (58) and (59) to Eqs. (55) and (56), we suppose that the right-hand side of equation is known and taken to be  $-f(x)e^{-Y}$ ; so, we have

$$\Psi_{YY} = -\omega^*, \quad (\text{B1})$$

$$\omega_{YY}^* = -f(x)e^{-Y}, \quad (\text{B2})$$

subject to

$$\Psi = \Psi_Y = 0 \quad \text{at } Y = 0, \quad (\text{B3})$$

$$\omega^* \rightarrow -g(x) \quad \text{as } Y \rightarrow \infty, \quad (\text{B4})$$

where both  $f(x)$  and  $g(x)$  are assumed to be known and finite. Thus, from (B2) and (B4), we have

$$\omega^* = -g(x) - f(x)e^{-Y}. \quad (\text{B5})$$

On the other hand, (B1) and (B4) imply that

$$\Psi_Y \sim Yg(x) + A(x) \quad \text{as } Y \rightarrow \infty,$$

where  $A(x)$  is to be determined. So, from Eqs. (B1) and (B5), we have

$$\Psi = \frac{1}{2}g(x)Y^2 + f(x)e^{-Y} + B(x)Y + C(x),$$

where  $B(x)$  and  $C(x)$  are also to be determined. Boundary conditions (B3) and (B4) then give

$$A(x) = B(x) = f(x), \quad C(x) = -f(x) - g(x),$$

so that  $A(x)$ ,  $B(x)$ , and  $C(x)$  are all determined.

Although this demonstrates that (B3) and (B4) constitute the requisite number of boundary conditions, it does not explain how to proceed if it is necessary to solve the problem numerically. To see this, note that even if (B2) is replaced by the more general form

$$\omega_{YY}^* = -h(x, Y),$$

where  $h(x, Y) \rightarrow 0$  as  $Y \rightarrow \infty$  sufficiently quickly so that (B4) is satisfied, we will have

$$\omega_Y^*(x, 0) = \int_0^\infty h(x, Y) dY.$$

So, for a numerical implementation, we would set

$$\Psi = 0, \quad \omega_Y^*(x, 0) = \int_0^\infty h(x, Y) dY \quad \text{at } Y = 0,$$

$$\omega^* \rightarrow -g(x), \quad \Psi_Y \sim Yg(x) + A(x) \quad \text{as } Y \rightarrow \infty,$$

where we iterate on  $A(x)$  until

$$\Psi_Y = 0 \quad \text{at } Y = 0.$$

**APPENDIX C: NUMERICAL SOLUTION FOR ASYMPTOTIC CORE FLOW**

Previously, Eq. (83) subject to (84)–(87) has been solved using pseudospectral and finite-difference methods;<sup>10,11</sup> in both cases, it was first necessary to take account of the singularities in the vorticity that are present at the corners of the rectangle. We also take account of these singularities, but use a finite-element method instead, as follows.

We split the vorticity up into a part that contains singularities,  $\omega^s$ , and one which does not,  $\omega^{ns}$ ; thus,  $\omega = \chi^{1/2}(\omega^s + \omega^{ns})$ , where

$$\omega^s = \omega_{0,0}(r_{0,0}, \theta_{0,0}) + \omega_{\lambda,0}(r_{\lambda,0}, \theta_{\lambda,0}) + \omega_{\lambda,1}(r_{\lambda,1}, \theta_{\lambda,1}) + \omega_{0,1}(r_{0,1}, \theta_{0,1}),$$

where

$$\omega_{0,0}(r_{0,0}, \theta_{0,0}) = r_{0,0}^{-1/2} \left( 3 \sin \frac{\theta_{0,0}}{2} - \cos \frac{\theta_{0,0}}{2} \right), \quad \omega_{\lambda,0}(r_{\lambda,0}, \theta_{\lambda,0}) = -r_{\lambda,0}^{-1/2} \left( 3 \cos \frac{\theta_{\lambda,0}}{2} - \sin \frac{\theta_{\lambda,0}}{2} \right),$$

$$\omega_{\lambda,1}(r_{\lambda,1}, \theta_{\lambda,1}) = -r_{\lambda,1}^{-1/2} \left( 3 \cos \frac{\theta_{\lambda,1}}{2} + \sin \frac{\theta_{\lambda,1}}{2} \right), \quad \omega_{0,1}(r_{0,1}, \theta_{0,1}) = r_{0,1}^{-1/2} \left( 3 \sin \frac{\theta_{0,1}}{2} + \cos \frac{\theta_{0,1}}{2} \right),$$

with

$$r_{0,0} = (x^2 + y^2)^{1/2}, \quad \theta_{0,0} = \tan^{-1} \left( \frac{y}{x} \right),$$

$$r_{\lambda,0} = ((x - \lambda)^2 + y^2)^{1/2}, \quad \theta_{\lambda,0} = \tan^{-1} \left( \frac{y}{x - \lambda} \right),$$

$$r_{0,1} = (x^2 + (y - 1)^2)^{1/2}, \quad \theta_{0,1} = \tan^{-1} \left( \frac{y - 1}{x} \right),$$

$$r_{\lambda,1} = ((x - \lambda)^2 + (y - 1)^2)^{1/2}, \quad \theta_{\lambda,1} = \tan^{-1} \left( \frac{y - 1}{x - \lambda} \right).$$

Setting also  $\hat{\psi} = \hat{\psi}^s + \hat{\psi}^{ns}$ , we have

$$\nabla^4 \hat{\psi}^{ns} = 0, \tag{C1}$$

subject to

$$\hat{\psi}_y^{ns} = -\hat{\psi}_y^s, \quad \hat{\psi}_x^{ns} (\hat{\psi}_{xx}^s + \hat{\psi}_{xx}^{ns}) + \hat{\psi}_x^s \hat{\psi}_{xx}^{ns} = -1 - \hat{\psi}_x^s \hat{\psi}_{xx}^s \quad \text{on } x = 0, \tag{C2}$$

$$\hat{\psi}_y^{ns} = -\hat{\psi}_y^s, \quad \hat{\psi}_x^{ns} (\hat{\psi}_{xx}^s + \hat{\psi}_{xx}^{ns}) + \hat{\psi}_x^s \hat{\psi}_{xx}^{ns} = 1 - \hat{\psi}_x^s \hat{\psi}_{xx}^s \quad \text{on } x = \lambda, \tag{C3}$$

$$\hat{\psi}_y^{ns} = -\hat{\psi}_y^s, \quad \hat{\psi}_x^{ns} = -\hat{\psi}_x^s \quad \text{on } y = 0, \tag{C4}$$

$$\hat{\psi}_y^{ns} = -\hat{\psi}_y^s, \quad \hat{\psi}_x^{ns} = -\hat{\psi}_x^s \quad \text{on } y = 1. \tag{C5}$$

To verify that  $\omega^{ns}$  is indeed free of singularities, it suffices to perform a local analysis about one of the corners; without loss of generality, we take (0,0). Thus, we have Eq. (C1) subject to, on suppressing the subscript “<sub>0,0</sub>,”

$$\hat{\psi}^{ns} = 0, \quad \hat{\psi}_\theta^{ns} = 0 \quad \text{at } \theta = 0,$$

$$\hat{\psi}^{ns} = 0, \quad \hat{\psi}_{\theta\theta}^s \hat{\psi}_\theta^{ns} + \hat{\psi}_\theta^s \hat{\psi}_{\theta\theta}^{ns} = 0 \quad \text{at } \theta = \pi/2,$$

which gives

$$\hat{\psi}^{ns} \sim r^q \left( \sin q\theta - \frac{q}{q-2} \sin(q-2)\theta - \left( \frac{q-1}{q-2} \right) (\cos q\theta - \cos(q-2)\theta) \tan \frac{1}{2}q\pi \right),$$

where  $q$  satisfies

$$(q-1)^2 \tan^2 \frac{q\pi}{2} + (q-1) \tan \frac{q\pi}{2} + q(q-2) = 0.$$

As observed by Roberts,<sup>10</sup>  $q = 3.5 \pm 0.7i, 3.5 \pm 0.7i, \dots$ , which indicates that  $\omega^{ns}$  will not be singular, since  $\omega^{ns} \sim r^{q-2}$ .

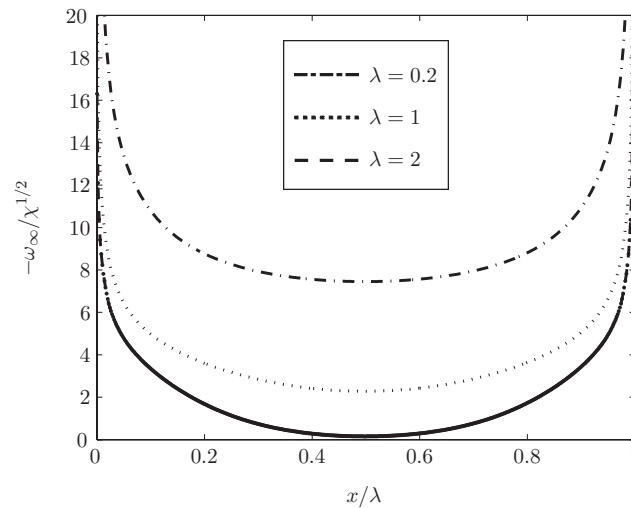


FIG. 18.  $-\omega_{\infty}/\chi^{1/2}$  vs.  $x/\lambda$  for  $\lambda = 0.2, 1, 2$ .

The remaining numerical task is the solution of (C1), subject to (C2)–(C5), which can be solved using the same finite-element method described in Sec. IV. To demonstrate how well the above splitting procedure works, we show in Fig. 18 the profiles obtained for  $-\omega_{\infty}/\chi^{1/2}$  vs.  $x/\lambda$  for  $\lambda = 0.2, 1, 2$ ; as is evident, our method gives a smooth oscillation-free profile for  $\omega_{\infty}$  as required for use in the boundary-layer computations.

- <sup>1</sup>L.-N. Moresi and V. S. Solomatov, “Numerical investigations of 2D convection with extremely large viscosity variations,” *Phys. Fluids* **7**(9), 2154–2162 (1995).
- <sup>2</sup>S. D. King, A. Raefsky, and B. H. Hager, “Conman: Vectorizing a finite element code for incompressible two-dimensional convection in the earth’s mantle,” *Phys. Earth Planet. Inter.* **59**, 195–207 (1990).
- <sup>3</sup>B. J. Travis, C. Anderson, J. Baumgardner, C. W. Gable, B. H. Hager, R. J. O’Connell, P. Olson, A. Raefsky, and G. Schubert, “A benchmark comparison for numerical methods for infinite Prandtl number thermal convection in two-dimensional Cartesian geometry,” *Geophys. Astrophys. Fluid Dyn.* **55**, 137–160 (1990).
- <sup>4</sup>B. Blankenbach, F. Busse, U. Christensen, L. Cserepes, D. Gunkel, U. Hansen, H. Harder, G. Jarvis, M. Koch, G. Marquart, D. Moore, P. Olson, H. Schmeling, and T. Schnaubelt, “A benchmark comparison for mantle convection codes,” *Geophys. J. Int.* **98**, 23–38 (1989).
- <sup>5</sup>S. D. King, “On topography and geoid from 2D stagnant lid convection calculations,” *Geochem., Geophys., Geosyst.* **10**, Q03002, doi:10.1029/2008GC002250 (2009).
- <sup>6</sup>P. E. van Keken, C. Currie, S. D. King, M. D. Behn, J. Cagnioncle, A. He, R. F. Katz, S.-C. Lin, E. M. Parmentier, M. Spiegelman, and K. Wang, “A community benchmark for subduction zone modeling,” *Phys. Earth Planet. Inter.* **171**, 187–197 (2008).
- <sup>7</sup>S. D. King, C. Lee, P. E. van Keken, W. Leng, S. Zhong, E. Tan, N. Tosi, and M. C. Kameyama, “A community benchmark for 2D Cartesian compressible convection in the Earth’s mantle,” *Geophys. J. Int.* **180**, 73–87 (2010).
- <sup>8</sup>D. E. Koglin, S. R. Ghias, S. D. King, G. T. Jarvis, and J. P. Lowman, “Mantle convection with reversing mobile plates: A benchmark study,” *Geochem., Geophys., Geosyst.* **6**, Q09003, doi:10.1029/2005GC000924 (2005).
- <sup>9</sup>P. E. van Keken, S. D. King, H. Schmeling, U. R. Christensen, D. Neumeister, and M.-P. Doin, “A comparison of methods for the modeling of thermochemical convection,” *J. Geophys. Res. - Solid Earth* **102**, 22477–22495, doi:10.1029/97JB01353 (1997).
- <sup>10</sup>G. O. Roberts, “Fast viscous Bénard convection,” *Geophys. Astrophys. Fluid Dyn.* **12**, 235–272 (1979).
- <sup>11</sup>J. Jimenez and J. A. Zufiria, “A boundary-layer analysis of Rayleigh-Bénard convection at large Rayleigh number,” *J. Fluid Mech.* **178**, 53–71 (1987).
- <sup>12</sup>A. C. Fowler, *Mathematical Geoscience* (Springer-Verlag, Berlin, 2011).
- <sup>13</sup>G. P. Chini and S. M. Cox, “Large Rayleigh number thermal convection: heat flux predictions and strongly nonlinear solutions,” *Phys. Fluids* **21**, 083603 (2009).
- <sup>14</sup>G. Veronis, “Large amplitude Bénard convection,” *J. Fluid Mech.* **26**, 49–68 (1966).
- <sup>15</sup>D. Turcotte and R. E. Oxburgh, “Finite amplitude convective cells and continental drift,” *J. Fluid Mech.* **28**, 29–42 (1967).
- <sup>16</sup>J. M. Strauss, “Finite amplitude double diffusive convection,” *J. Fluid Mech.* **56**, 353–374 (1972).
- <sup>17</sup>D. R. Moore and N. O. Weiss, “Two-dimensional Rayleigh-Bénard convection,” *J. Fluid Mech.* **58**, 289–312 (1973).
- <sup>18</sup>P. Olson and G. M. Corcos, “A boundary layer model for mantle convection with surface plates,” *Geophys. J. R. Astron. Soc.* **62**, 195–219 (1980).
- <sup>19</sup>S. Grossmann and D. Lohse, “Scaling in thermal convection: A unifying theory,” *J. Fluid Mech.* **407**, 27–56 (2000).
- <sup>20</sup>S. Grossmann and D. Lohse, “Thermal convection for large Prandtl numbers,” *Phys. Rev. Lett.* **86**, 3316–3319 (2001).